High-Resolution Model-Based Investigation of Moisture Transport into the Pacific Northwest during a Strong Atmospheric River Event

MICHAEL J. MUELLER

Cooperative Institute for Research in the Environmental Sciences, and NOAA/Earth System Research Laboratory, Boulder, Colorado

KELLY M. MAHONEY

Physical Sciences Division, NOAA/Earth System Research Laboratory, Boulder, Colorado

MIMI HUGHES

Cooperative Institute for Research in the Environmental Sciences, and NOAA/Earth System Research Laboratory, Boulder, Colorado

(Manuscript received 8 December 2016, in final form 26 June 2017)

ABSTRACT

A series of precipitation events impacted the Pacific Northwest during the first two weeks of November 2006. This sequence was punctuated by a particularly potent inland-penetrating atmospheric river (AR) that produced record-breaking precipitation across the region during 5–7 November. The precipitation caused destructive flooding as far inland as Montana's Glacier National Park, 800 km from the Pacific Ocean. This study investigates the inland penetration of moisture during the event using a 4–1.33-km grid spacing configuration of the Weather Research and Forecasting (WRF) modeling system. A high-resolution simulation allowed an analysis of interactions between the strong AR and terrain features such as the Cascade Mountains and the Columbia River Gorge (CR Gorge).

Moisture transport in the vicinity of the Cascades is assessed using various metrics. The most efficient pathway for moisture penetration was through the gap (i.e., CR Gap) between Mt. Adams and Mt. Hood, which includes the CR Gorge. While the CR Gap is a path of least resistance through the Cascades, most of the total moisture transport that survived transit past the Cascades overtopped the mountain barrier itself. This is due to the disparity between the length of the ridge (~800 km) and relatively narrow width of the CR Gap (~93 km). Moisture transport reductions were larger across the Washington Cascades and the southern-central Oregon Cascades than through the CR Gap. During the simulation, drying ratios through the CR Gap (9.3%) were notably less than over adjacent terrain (19.6%–30.6%). Drying ratios decreased as moisture transport intensity increased.

1. Introduction

The western United States is vulnerable to destructive flooding events due to steep terrain, rocky soil, snow, and ice cover especially prevalent at higher elevations. Flooding events are often caused by heavy precipitation falling on these surfaces, contributing rapid runoff to rivers and streams. Such heavy precipitation events are often associated with long, narrow filaments of enhanced vertically integrated water vapor transport (IVT) known as atmospheric rivers (ARs) (e.g., Newell et al. 1992; Newell and Zhu 1994; Ralph et al. 2004). This study seeks to quantify inland moisture transport and airmass drying across complex terrain during a major landfalling AR event in the Pacific Northwest using a high-resolution numerical model. Thus, this paper complements previous research that used coarser datasets by conducting a case study analysis using a high-resolution dataset.

Climatologically, ARs commonly occur in the warm sector of extratropical cyclones. They are prominent features of the global water cycle as they account for over 90% of extratropical poleward water vapor transport (Zhu and Newell 1998). As such, they have a large impact on the availability of water resources in heavily

Corresponding author: Michael J. Mueller, michael.mueller@noaa.gov

DOI: 10.1175/MWR-D-16-0466.1

populated and otherwise semiarid or arid locations such as Southern California (Dettinger et al. 2011). They are also important for their association with high-impact orographic precipitation events as they impinge upon mountain ranges.

Although ARs have been documented in various regions of the world like the southeastern United States (e.g., Moore et al. 2012; Lackmann 2013; Moore et al. 2015; Mahoney et al. 2016), central United States (Lavers and Villarini 2013), and Europe (Stohl et al. 2008; Lavers and Villarini 2015; Ramos et al. 2015), they have been most extensively studied in the northeastern Pacific and western North America (e.g., Dettinger 2004; Neiman et al. 2008a, 2013; Leung and Qian 2009; Smith et al. 2010; Rutz and Steenburgh 2012; Dettinger 2013; Hughes et al. 2014; Alexander et al. 2015; Behrangi et al. 2016; Ralph et al. 2005, 2006, 2011, 2013). While ARs are associated with a large proportion of cool season precipitation in the western United States, the total fraction (known as "AR fraction") varies based on location. Cooperative Observer Program (COOP) and snowpack telemetry (SNOTEL) data revealed AR fractions of 20%–50% in California, Oregon, and Washington (Dettinger et al. 2011; Rutz and Steenburgh 2012). Rutz et al. (2014) found AR fractions of 50%–60% with lower values inland, especially to the lee of the high Sierra Nevada (<10%). The AR fractions at interior locations such as the Columbia River basin (CRB) and the western Montana Rockies decreased to 35% and 25%, respectively. Such relative interior maxima led Rutz et al. (2015) to identify three main flow regimes associated with moisture penetration pathways both north and south of the high Sierras. These findings support Alexander et al. (2015), which showed a tendency for ARs to penetrate farther inland across the Pacific Northwest and U.S. Southwest due to moisture transport through gaps in or around higher upwind terrain.

Case studies of inland-penetrating ARs provide additional motivation to understand the physical controls on moisture transport that may lead to inland flooding. Hughes et al. (2014) examined the impact of upwind terrain height on total moisture flux in Arizona during an inland-penetrating AR in January 2010. Moisture removal was demonstrated to be more extensive upon AR interaction with high terrain, helping to explain why AR fractions are lower downwind of mountain ranges. The relationship between terrain height and moisture removal is not as well studied for other regions of the U.S. Intermountain West, yet the potential for inland-penetrating ARs to cause high-impact precipitation is high. The present study investigates moisture pathways through the Pacific Northwest during a high-impact, inland-penetrating AR event.

In early November 2006, a sequence of ARs generated record-breaking precipitation across the Pacific Northwest (Neiman et al. 2008b). An especially intense AR transported moisture-laden air into Washington and Oregon, causing heavy precipitation as it impinged on the Olympic and Cascade Mountains. While a portion of the moisture fell as orographic precipitation on the western slopes of mountain ranges in western Washington and Oregon, a large portion continued to push into the interior west. Record rainfall and destructive flooding occurred 800 km inland at Montana's Glacier National Park (Bernhardt 2006).

This study uses a high-resolution modeling approach to better understand how moisture from the AR penetrated the Pacific Northwest during this case. Specifically, our objectives are to address the following science questions:

1) Where were the primary corridors for inland moisture penetration?
2) How much moisture traveled through the corridors in comparison to over adjacent terrain?
3) What proportion of upstream moisture flux was lost during transit through the corridors?

The case studied here was chosen as an example of an intense, high-impact moisture transport and precipitation event east of the Cascades. In addition, the AR's orientation was similar to previously identified routes through the region [e.g., regime 1 of Rutz et al. (2015)], suggesting the case is well suited to address our questions.

2. Methods

a. *Model configuration*

High-resolution regional models have proven useful to investigate physical processes (e.g., Keyser and Uccellini 1987). In this study, the Advanced Research Weather Research and Forecasting (WRF-ARW), version 3.8.1 (Skamarock et al. 2008), modeling system was used to generate a high-resolution dataset with which to investigate moisture transport through the Pacific Northwest. Simulations were conducted during 0000 UTC 3 November–0000 UTC 9 November 2006. Model initial and lateral boundary conditions were provided by 6-hourly Climate Forecast System Reanalysis (CFSR) data. The CFSR is a global dataset with resolution of T382 (~38 km) with 64 vertical levels (Saha et al. 2010).

Two nested WRF domains were configured over western North America and the northeast Pacific Ocean (Fig. 1). The outer (inner) domain had a horizontal grid spacing of 4 (1.33) km and 54 terrain-following vertical levels. Lateral boundary conditions for the inner domain

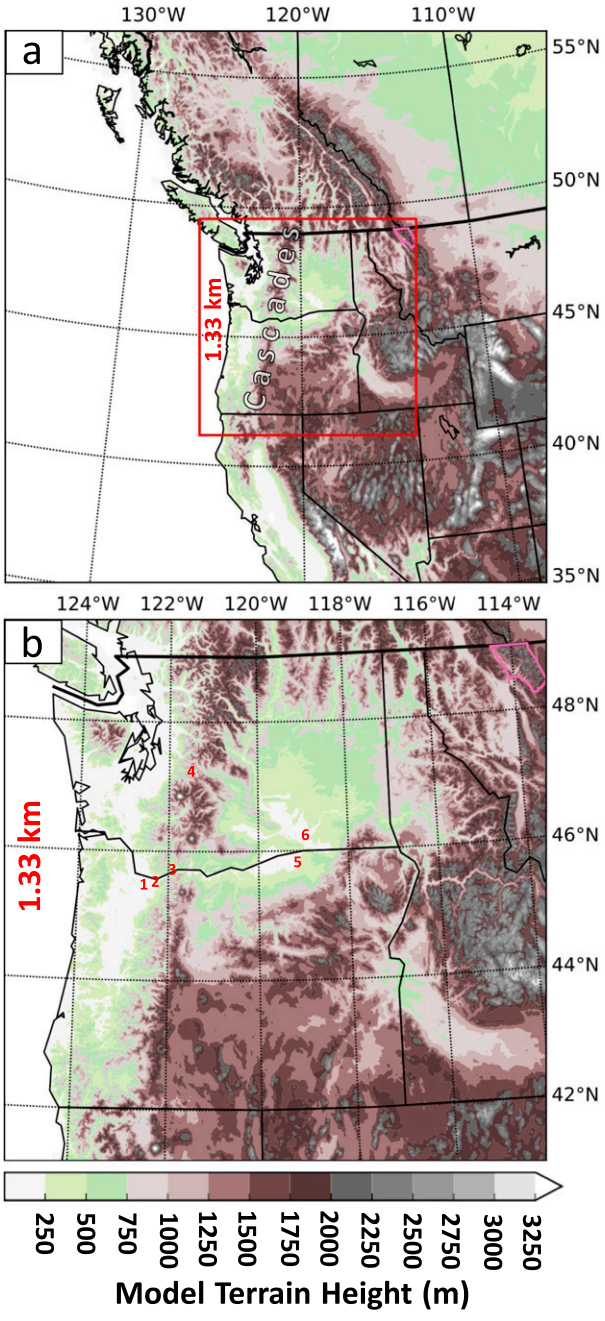

FIG. 1. WRF Model terrain height on (a) outer 4-km domain and (b) inner 1.33-km domain. The Cascades are labeled and the 1.33-km domain outlined in (a). Glacier National Park is outlined in pink for context. In (b), observing station locations are shown at 1) Portland, OR (PDX); 2) Troutdale, OR (TTD); 3) Cascade Locks, OR (CZK); 4) Stampede Gap, WA (SMP); 5) Hermiston, OR (HMI); and 6) Pasco, WA (PSC).

were derived from the outer domain, but there was no feedback from the inner domain to the outer domain.

A 12–4-km WRF configuration was used to investigate the sensitivity of the simulation to downscaling from 38-km CFSR data to the 4-km WRF mesh. Differences between the inner 4-km grid (not shown) and the outer 4-km grid (used in this study) were minor and imply directly forcing the 4-km domain with CFSR data is acceptable during this 6-day case.

The 1.33-km WRF mesh was used to adequately resolve mesoscale flow patterns typical of the Pacific Northwest and Columbia River Gorge (CR Gorge) region (e.g., Sharp and Mass 2002). Orographic features critical to precipitation enhancement and water vapor removal like the Cascades and the CR Gorge were clearly resolved. Both 4- and 1.33-km grid spacing allowed explicit modeling of cumulus convection impacts, avoiding the need to use a cumulus parameterization scheme. Additional model physics options are summarized in Table 1.

We used 4- and 1.33-km domains to show the evolution of the AR at the synoptic and mesoscale, respectively. Both domains are used to assess the resolution dependence of results, especially with respect to surface winds in the vicinity of the Cascades and CR Gorge. The 1.33-km domain was used exclusively to compute water vapor and total moisture transport through the Pacific Northwest.

b. *Model verification*

Because the goal of this study was to closely examine moisture transport, it was necessary to verify related model output like precipitation and wind with observation-based information. Therefore, a gridded precipitation dataset based on NOAA's COOP observations (Livneh et al. 2013, hereafter "Livneh precipitation data") was used to verify spatial distribution and magnitude of model precipitation. The verification dataset covers the continental United States and the Columbia River watershed in Canada and is on a 1/16° grid ($\Delta x \sim 5$ km, $\Delta y \sim 7$ km).

To assess wind flow across the Cascades and through various gaps in the terrain (i.e., the CR Gorge and Stampede Gap), model 10-m wind speed and direction were compared to observed wind at six locations (Fig. 1b): 1) Portland, Oregon (PDX); 2) Troutdale, Oregon (TTD); 3) Cascade Locks, Oregon (CZK); 4) Stampede Gap, Washington (SMP); 5) Hermiston, Oregon (HRI); and 6) Pasco, Washington (PSC). These data also served to examine low-level easterly winds through the CR Gorge, a pattern that often precedes AR landfall and associated west–east moisture transport across the Cascades (e.g., Sharp and Mass 2002).

c. *Moisture transport calculations*

To quantify moisture transport through the Pacific Northwest, we computed integrated water vapor (IWV),

TABLE 1. WRF namelist options for both 4-km and 1.33-km grids.

Field	Option
Grid points	599 × 599 (4 km); 700 × 700 (1.33 km)
Model top	10 hPa
Microphysics	Thompson (Thompson et al. 2008)
Longwave radiation	RRTM (Mlawer et al. 1997)
Shortwave radiation	Dudhia (Dudhia 1989)
Surface layer	Monin–Obukhov
Land surface model	Noah (Ek et al. 2003)
Planetary boundary layer	Yonsei University (YSU) (Hong et al. 2006)
Cumulus	None

integrated water vapor transport (IVT), integrated water transport (IWT), and moisture mass transport (QT). We used IWV to reveal the total amount of water vapor in an atmospheric column available for precipitation:

$$\mathrm{IWV} = \frac{1}{g}\int_{\mathrm{sfc}}^{200\mathrm{hPa}} q_{\mathrm{vap}}\, dp, \tag{1}$$

where g is the gravitational acceleration, p is the pressure level, and q_{vap} is the mixing ratio of water vapor to dry air (Rutz et al. 2014). Water vapor mixing ratios were interpolated to constant pressure levels at 25-hPa intervals, and then averaged over each vertical layer. Layer-averaged mixing ratios were summed from the surface to 200 hPa to calculate IWV.

Water vapor transport was quantified through IVT, a vertically integrated horizontal water vapor flux calculated in this paper as

$$\mathrm{IVT} = \frac{1}{g}\int_{\mathrm{sfc}}^{200\mathrm{hPa}} q_{\mathrm{vap}}\mathbf{U}\, dp, \tag{2}$$

where $\mathbf{U}$ is the total wind vector including both zonal (u) and meridional (v) wind components, and other variables are as in Eq. (1) (Rutz et al. 2014). Both q_{vap} and $\mathbf{U}$ were interpolated to constant pressure levels as in the IWV calculation. IVT was calculated on each pressure level and averaged over 25-hPa vertical layers. Layer averages were summed to compute IVT (which has units of $\mathrm{kg\,m^{-1}\,s^{-1}}$). A closely related metric—IWT—was calculated exactly as IVT, except using the combined mixing ratio for all six water species (i.e., water vapor, cloud, rain, snow, ice, and graupel) produced by the Thompson microphysics scheme (Thompson et al. 2008).

We used IWT to calculate the impact of the Cascades on moisture transport, applying the drying ratio (DR) described in Kirshbaum and Smith (2008) in which total upstream moisture transport was compared to total moisture transport downstream of a barrier. In this study, drying ratios were calculated with respect to the Cascades:

$$\mathrm{DR} = 1 - \frac{\mathrm{IWT}_{\mathrm{downstream}}}{\mathrm{IWT}_{\mathrm{upstream}}}. \tag{3}$$

A DR of 1 signaled total drying of the atmosphere, while a DR of 0 signaled no drying. Four corridors were defined across the Cascades to denote upstream and downstream regions (see Fig. 13). A caveat to the static corridor approach is that due to shifts in wind direction, some moisture transport that is recorded downwind of the Cascades may not be recorded upwind of the Cascades (and vice versa). This results in occasional negative drying ratios. We mitigated this impact by defining southwest–northeast-oriented corridors aligned with the general flow; however, fluctuations in transport direction near the end of the AR event briefly produced $\mathrm{IWT}_{\mathrm{downstream}} > \mathrm{IWT}_{\mathrm{upstream}}$.

Finally, to directly quantify total water vapor mass transport and total moisture mass transport we computed the following:

$$\mathrm{QT}_{\mathrm{vap}} = \Delta x \int_{t_0}^{t_f} |\mathrm{IVT}|\, dt, \tag{4}$$

$$\mathrm{QT}_{\mathrm{mois}} = \Delta x \int_{t_0}^{t_f} |\mathrm{IWT}|\, dt, \tag{5}$$

where Δx is horizontal model grid spacing in meters, t_f is the end of a specified time period, and t_0 is the beginning of the time period. Integrating horizontal flux terms over time and multiplying by grid spacing yields water mass transport, a quantity we used to examine the total amount of moisture that flowed through the Pacific Northwest. We also plotted time-integrated water vapor and moisture transport vertical cross sections to investigate the vertical structure of the AR interacting with and flowing over the Cascades. These quantities are denoted $\mathrm{QTV}_{\mathrm{vap}}$ and $\mathrm{QTV}_{\mathrm{mois}}$ to differentiate with the vertically integrated quantity QT. Zonal and meridional components of these quantities are denoted $\mathrm{uQTV}_{\mathrm{vap}}$, $\mathrm{vQTV}_{\mathrm{vap}}$, $\mathrm{uQTV}_{\mathrm{mois}}$, and $\mathrm{vQTV}_{\mathrm{mois}}$.

Finally, we used $\mathrm{QT}_{\mathrm{vap}}$ and $\mathrm{QT}_{\mathrm{mois}}$ to calculate total moisture breaching the ridge of the Cascades. We separated the ridge into six distinct terrain-based segments to quantify how much moisture was transported across the ridge in those regions (see Fig. 13). The segments are distinct from the four corridors used to calculate DR as they were designed to examine different aspects of moisture transport across the Cascades. The gap between Mt. Adams and Mt. Hood (i.e., the Columbia River Gap, hereafter CR Gap), which includes the CR Gorge, is a special focus of this study.

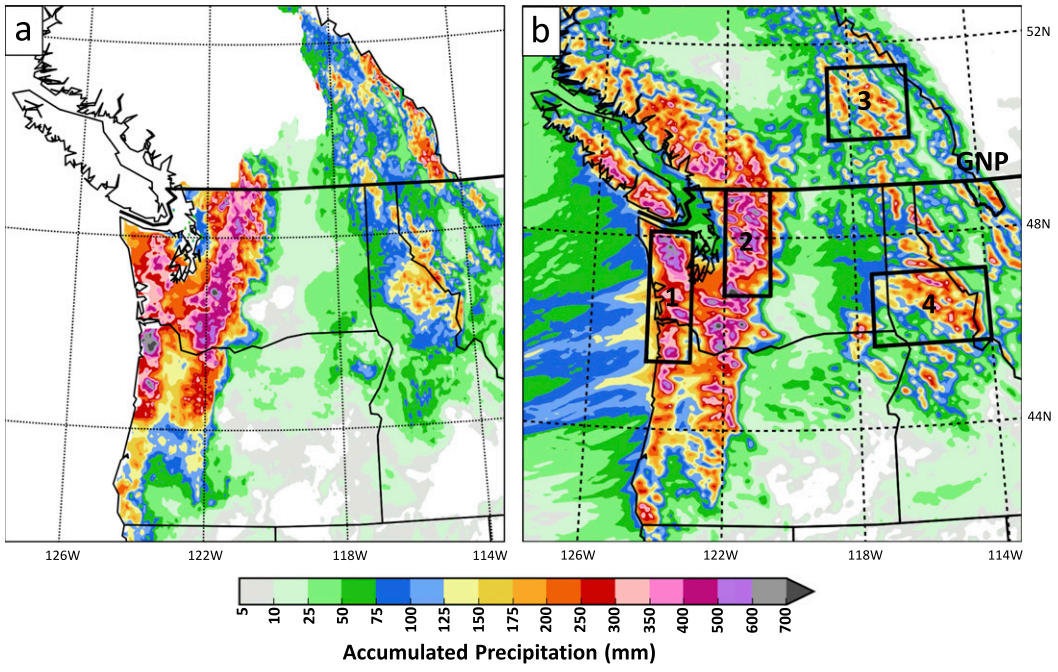

FIG. 2. The 6-day accumulated precipitation from (a) Livneh et al. (2013) observation-based dataset and (b) 4-km WRF simulation. Four regions for area-averaging plus Glacier National Park are outlined in black and labeled.

3. Case description and model verification

a. Precipitation and synoptic overview

The 6-day 4-km WRF accumulated precipitation and Livneh precipitation data (Fig. 2) revealed two areas of heavy precipitation: 1) over the coastal mountains near the Pacific Ocean (i.e., Cascade, Olympic, and Coastal ranges) and 2) over the interior mountains (e.g., the Canadian Rockies and Sawtooth Mountains). Precipitation magnitudes were similar in both WRF and Livneh datasets. Widespread precipitation accumulations over the Coastal and Cascade Mountains exceeded 300 mm with some locations exceeding 600 mm near individual high mountains and ridges. Over interior mountains, widespread 125–175-mm accumulations occurred with areas that exceeded 250 mm along higher ridges. Precipitation minima of less than 50 mm were located immediately east of the Cascades and in mountain valleys in Idaho, Montana, and British Columbia.

Area-averaged hourly 4-km WRF accumulated precipitation and daily Livneh precipitation data were computed for five regions selected over areas (shown in Fig. 2b) of heavy precipitation (Fig. 3). WRF and Livneh precipitation were similar in terms of both magnitude and timing. All regions experienced 24–36 h of persistent heavy precipitation from 6 to 8 November, consistent with case descriptions in Neiman et al. (2008b) and Bernhardt (2006). Interior and southern regions experienced precipitation onset about 12–15 h after coastal regions. In addition to the primary event, 25–125 mm of antecedent precipitation fell in association with a weaker AR from 3 to 5 November. The heaviest antecedent amounts fell along the Coastal and Cascade Mountains.

At 0000 UTC 7 November, 4-km WRF showed a ridge anchored over the California coast at 300 and 700 hPa (Fig. 4). A longwave trough existed northwest of the ridge. The resultant geopotential height gradient at 300 hPa was associated with a >150-kt (1 kt = 0.5144 m s^{-1}) jet streak just north of the U.S.–Canadian border. The Pacific Northwest was located under the lift-unfavorable right exit region of the jet streak while the heaviest precipitation fell. At 700 hPa, a long, narrow band of nearly saturated air extended from the Pacific Ocean to the interior of the Pacific Northwest. Strong 50–70-kt winds advected moisture toward areas of heavy precipitation in the mountains of Washington, Oregon, Idaho, and Montana. Accumulated precipitation distribution and mid- and upper-level synoptic patterns suggest low-level moisture convergence near higher terrain was a key factor in precipitation enhancement during the event.

At the same time, the 1.33-km grid showed enhanced moisture (q_{vap} = 11–12 g kg^{-1}) and 20–40 kt winds from western Oregon and Washington across the Cascades

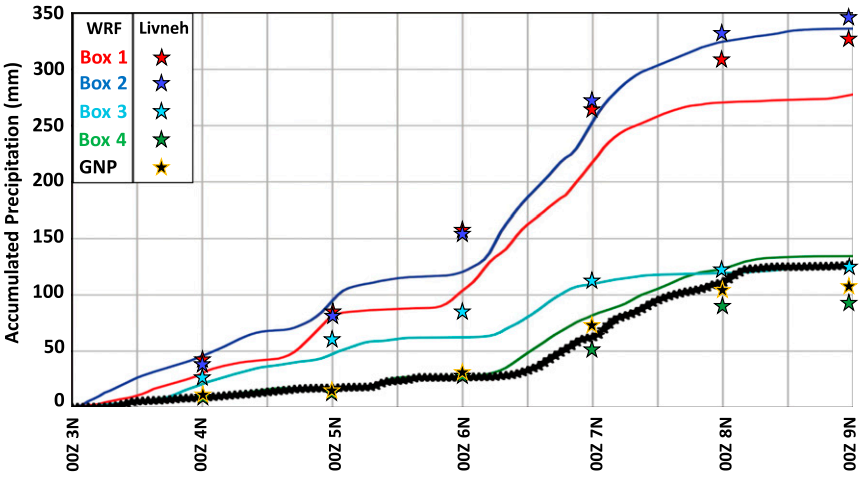

FIG. 3. Temporal plumes of area-averaged 4-km WRF accumulated precipitation (lines) and daily Livneh precipitation (stars) at five regions depicted in Fig. 2b.

into eastern Washington, northern Idaho, and western Montana. Enhanced moisture (q_{vap} = 9–11 g kg^{-1}) existed well into the interior mountains. The highest interior 2-m water vapor mixing ratios were located in the CR Gap at this time—the likely result of terrain effects and the location of the AR core. West–east moisture transport persisted until 1200 UTC 7 November (not shown); precipitation rapidly diminished across the Pacific Northwest at this time.

b. *Surface winds*

Since low-level winds through the CR Gorge tend to be from the east as ARs approach (a dry flow; e.g., Sharp and Mass 2002), we examined a sequence of 12-h averaged 10-m zonal wind during the primary AR event (1200 UTC 5 November–1200 UTC 8 November). Results from both 4-km and 1.33-km grids were used to ensure adequate resolution of gorge flow and to explore the value added by the 1.33-km simulation (Fig. 5). Both resolutions indicate westerly winds through the CR Gorge, especially near its western outlet where climatology indicates easterlies would be strongest. While these model-derived plots indicate flow through the CR Gorge was generally westerly during the AR, 12-h time averaging could obscure the finely detailed mesoscale progression of winds typical of the region.

Hourly model time series of wind speed and direction were compared to observations at six locations (Figs. 6 and 7). Both wind speed and direction show general agreement between model simulations (4 and 1.33 km)

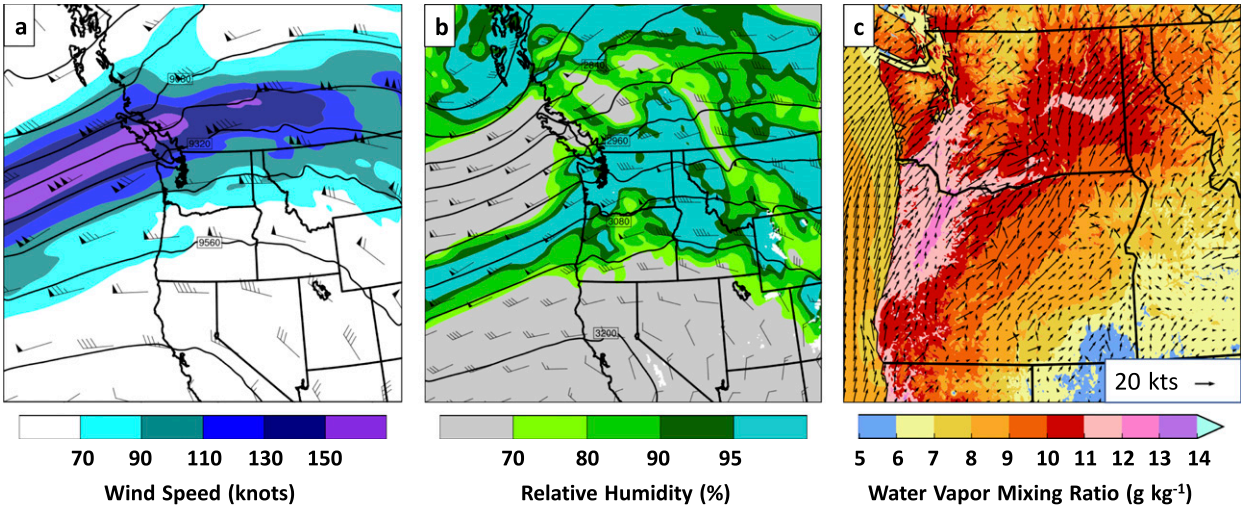

FIG. 4. Model synoptic charts at 0000 UTC 7 Nov: (a) 4-km WRF 300-hPa geopotential height, wind, and isotachs; (b) 4-km WRF 700-hPa geopotential height, wind, and relative humidity; and (c) 1.33-km WRF 2-m water vapor mixing ratio and 10-m wind.

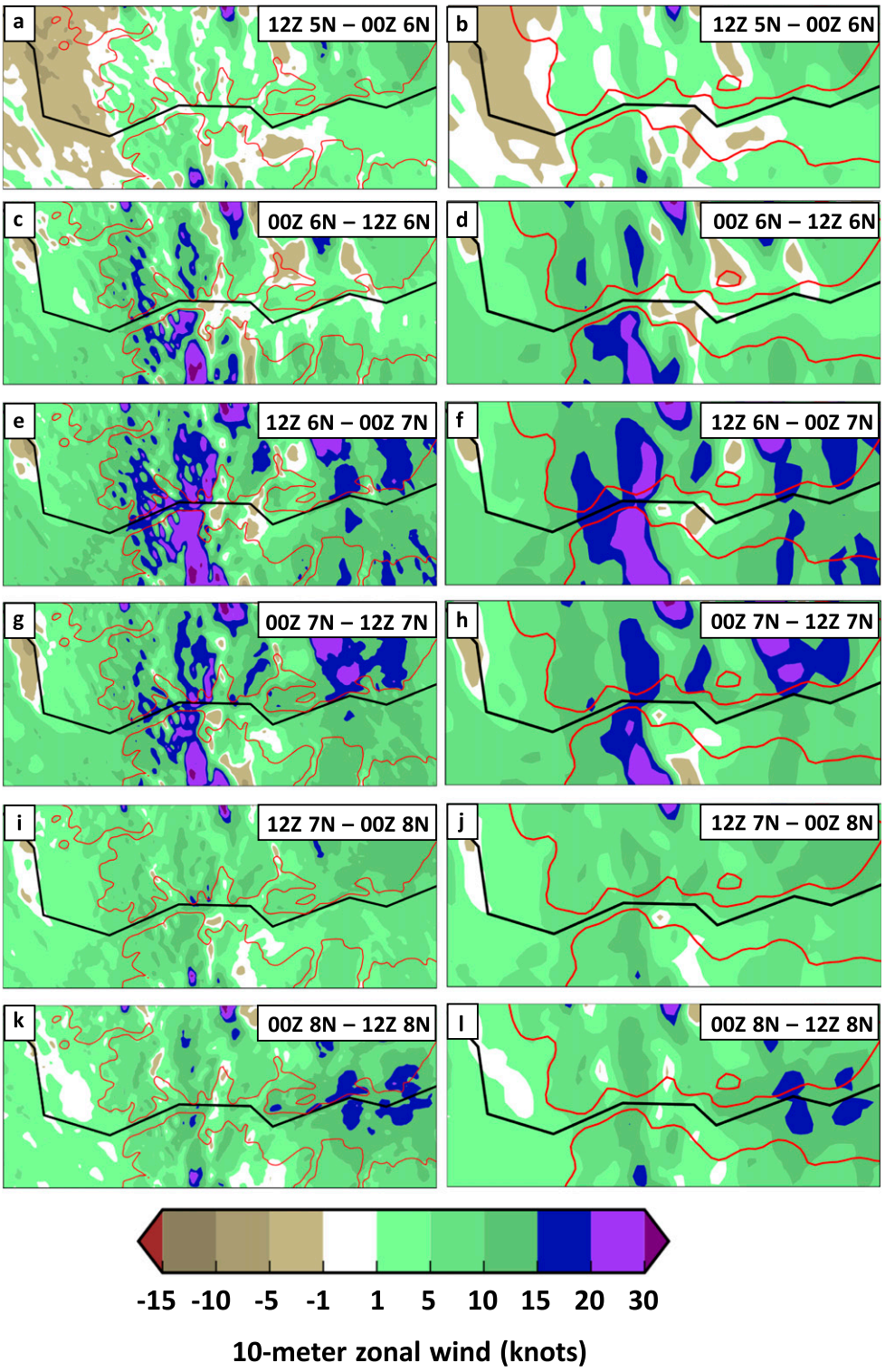

FIG. 5. Time-averaged zonal winds at 10 m AGL from (left) 1.33-km WRF and (right) 4-km WRF. Positive values denote the westerly component of the wind. The 500-m terrain contour is drawn in red to show the location of the CR Gorge. The WA–OR border is drawn in black.

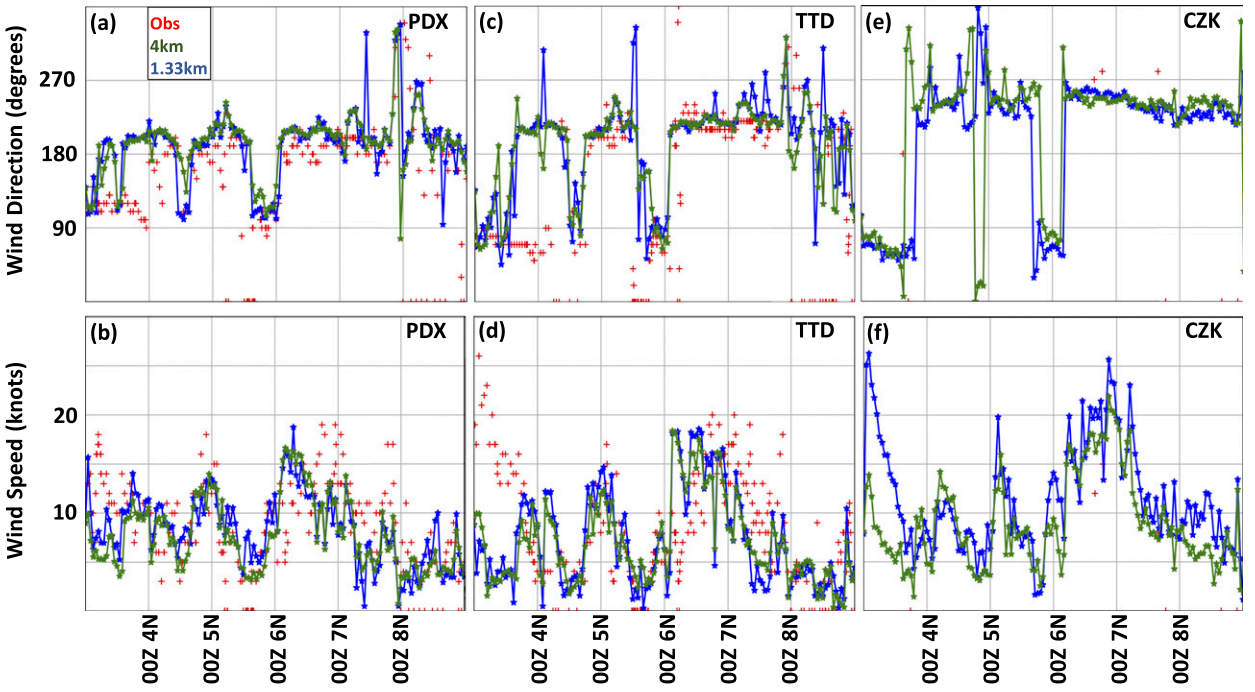

FIG. 6. Model and observed (red crosses) 10-m wind direction and speed at (a),(b) Portland, OR (PDX); (c),(d) Troutdale, OR (TTD); and (e),(f) Cascade Locks, OR (CZK). Green traces denote 4-km WRF wind data; blue traces denote 1.33-km WRF wind data.

and observations. As expected, weak easterly winds occurred for several hours prior to AR impact, especially at PDX, TTD, and CZK—locations within the CR Gorge or immediately west of its western outlet. Although there were few observations at CZK, the existing observations agreed with model output. Furthermore, the location provides an excellent opportunity to examine winds in the western half of the CR Gorge. After ~0300 UTC 6 November, winds at these three locations shifted to the south-southwest and remained from this direction until the AR event ended. The wind evolution through the Stampede Gap (SMP) was similar to wind evolution through the CR Gorge, albeit with more variability on the 1.33-km grid. Model and observation data in the CRB at HRI and PSC featured south-southwesterly winds during much of the primary AR event.

c. *IWV*

WRF 4-km vertically integrated water vapor (IWV) shows the approach, landfall, inland penetration, and decay of the primary AR (Fig. 8). The AR reached its maximum intensity during 1200 UTC 6 November–0000 UTC 7 November with IWV values of 4–5 cm along the coast. Local maxima of IWV existed in the CRB east of the Cascades, suggesting inland penetration of water vapor. Inland IWV patterns were influenced by both moisture removal via precipitation and routing of low-level moisture through paths of least resistance (i.e., river valleys and other regions of low terrain). The AR propagated southward along the coast and decayed following the occlusion of its parent cyclone.

Time-averaged 12-hourly vertical water vapor mixing ratio profiles show the evolution of the moist column over Troutdale, just west of the CR Gorge (Fig. 9). The atmospheric column shows moisture magnitude and depth increased as the AR approached and decreased as it decayed and moved south of Troutdale. Half of all water vapor mass remained under 850 hPa even during the most intense 12-h period of the AR. Only 10% (20%) of total column water vapor existed above 700 hPa after AR passage (during the height of the AR). While much of the water vapor mass remained at Cascades ridge level or below (~870 hPa), water vapor (and total moisture) advection by wind at all levels was the mechanism for water vapor (moisture) transport as defined in Eq. (2).

4. Moisture transport

a. *IVT*

We began our investigation of moisture transport by examining vertically integrated water vapor transport on the 4-km WRF grid (IVT; Fig. 10). At 1200 UTC 5 November, the primary AR core resided well offshore while remnants of the decaying antecedent AR

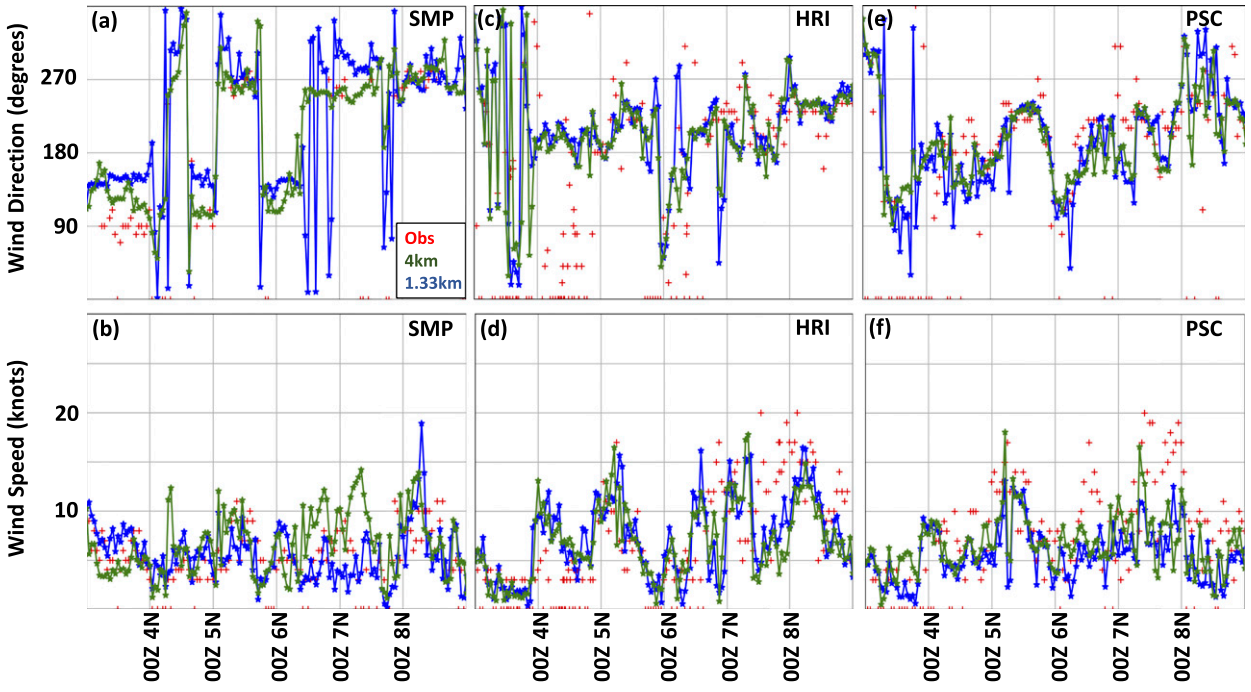

FIG. 7. As in Fig. 6, but at (a),(b) Stampede Gap, WA (SMP); (c),(d) Hermiston, OR (HRI); and (e),(f) Pasco, WA (PSC).

extended from southwestern Oregon northeastward into Montana, Alberta, and Saskatchewan, Canada. The 600 kg m^{-1} s^{-1} IVT contour associated with the primary AR made landfall along the Washington and Oregon coasts prior to 0000 UTC 6 November. IVT vectors were oriented from the west-southwest to the east-northeast, a pattern that changed little during the event. The IVT vector orientation—which strongly resembled routes for interior penetrating ARs presented in Rutz et al. (2015)—favored water vapor transport across the Cascades, especially in the vicinity of the CR Gap.

By 1200 UTC 6 November, IVT values greater than 600 kg m^{-1} s^{-1} had reached the interior mountains. IVT exceeded 1100 kg m^{-1} s^{-1} along the Washington–Oregon coasts and in a narrow corridor through the CR Gap. Water vapor transport attenuation appeared minimal through and downwind of the CR Gap; however, IVT clearly penetrated over the Cascades at all latitudes. The largest IVT decreases appeared to occur across the Olympics–Cascades double barrier in northern Washington. Slightly enhanced IVT occurred through the Stampede Gap and other localized depressions in the Cascades ridge.

At 0000 UTC 7 November, the corridor of maximum IVT flowed in the vicinity of the CR Gap and CRB en route to the interior mountains. Intense interior precipitation was occurring at this time, a likely response to strong water vapor transport impinging on regional mountain barriers. IVT weakened during the following 24 h: maximum offshore values decreased from approximately 1400 kg m^{-1} s^{-1} at 0000 UTC 7 November to 700 kg m^{-1} s^{-1} by 0000 UTC 8 November.

Interior IVT was still robust at 1200 UTC 7 November (600–800 kg m^{-1} s^{-1} from the Cascades to Montana). Strong interior water vapor transport suggested the mountain barrier over the northern third of Oregon did not impede penetration as much as the mountain barrier in Washington. By 0000 UTC 8 November, the AR moved south to the Oregon–California border and weakened. Interior IVT values exceeding 600 kg m^{-1} s^{-1} became much less widespread. Precipitation over the interior mountains was rapidly ending by this time, likely in response to regional IVT decline.

Time-averaged 12-hourly water vapor transport profiles show the evolution of water vapor transport over Troutdale (Fig. 11). Water vapor transport profiles notably differ from those of water vapor mass (see Fig. 9) due to the influence of wind. Water vapor transport values were greatest from about 950 to 600 hPa. During 0000 UTC 6 November–0000 UTC 7 November, very intense low-level water vapor transport centered on ~900 hPa. The layer of greatest transport broadened considerably after 0000 UTC 7 November. The increased depth of transport is clearly depicted in Fig. 11b. About 70% of water vapor transport occurred above the

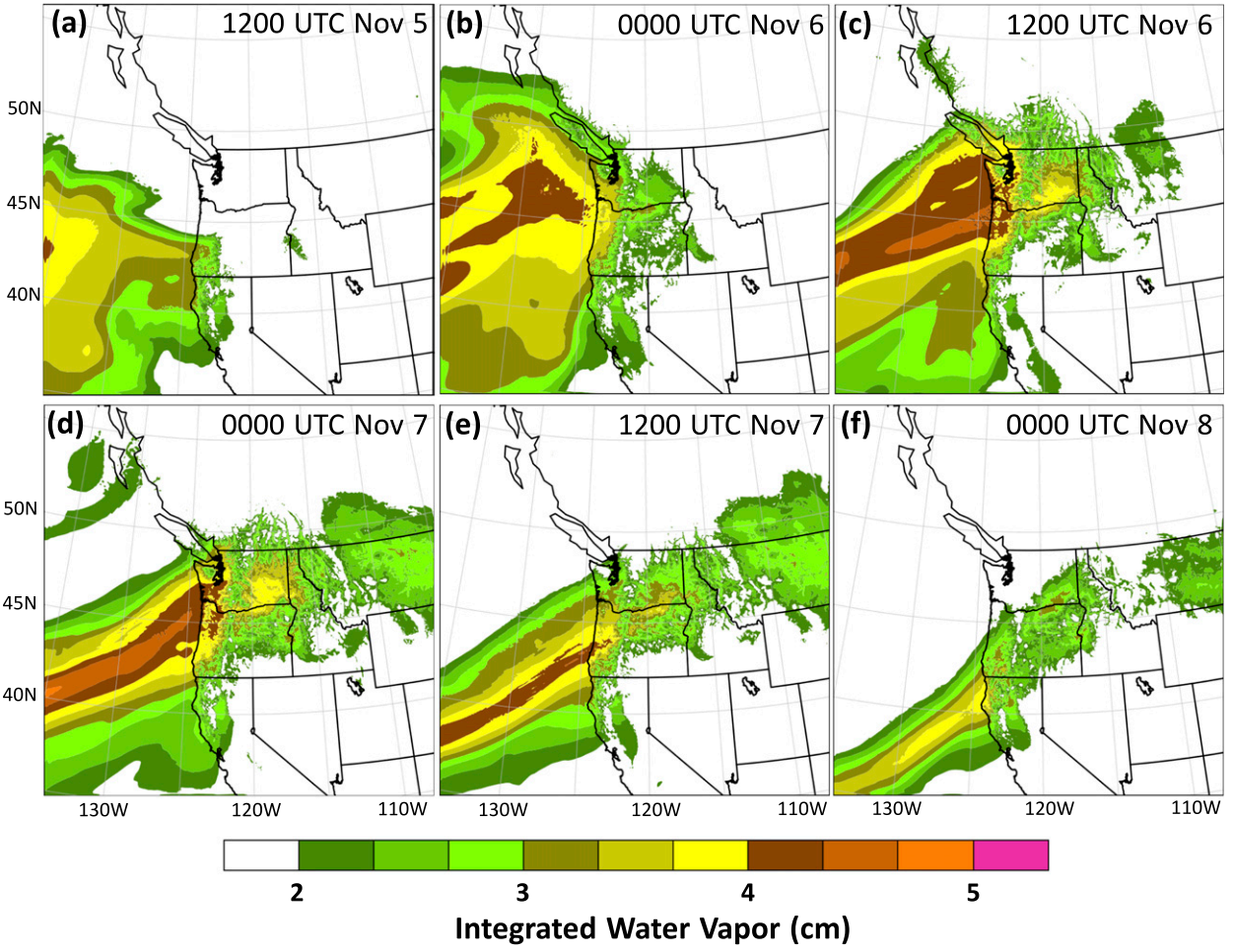

FIG. 8. Plan views of WRF 4-km integrated water vapor (IWV, in cm) at (a) 1200 UTC 5 Nov, (b) 0000 UTC 6 Nov, (c) 1200 UTC 6 Nov, (d) 0000 UTC 7 Nov, (e) 1200 UTC 7 Nov, and (f) 0000 UTC 8 Nov.

average Cascades ridge height (~870 hPa) during the early stages of the AR event (0000 UTC 6 November–1200 UTC 6 November). About 83% occurred above the ridge during the later stages (1200 UTC 7 November–0000 UTC 8 November). Above 700 hPa, 30% (55%) of vapor transport occurred during the early stages (later stages) of the AR event.

WRF 4-km time-integrated water vapor transport (water vapor mass transport, QT_{vap}) over the life cycle of the primary AR—1200 UTC 5 November–1200 UTC 8 November—revealed the main corridor of water vapor transport through the Pacific Northwest (Fig. 12). Over 7×10^{11} kg of water vapor flowed from the Pacific Ocean to the Oregon and Washington coasts. The Olympics and Cascades were clear impediments to inland water vapor penetration with only small QT_{vap} reductions across the Coastal Ranges. Maximum inland QT_{vap} flowed through the CR Gap and CRB en route to northern ID and western Montana. The QT_{vap} in the CRB was $5–7 \times 10^{11}$ kg, a reduction of 15%–30% across the Cascades. To the lee of the Montana Rockies, QT_{vap} was $4–5 \times 10^{11}$ kg, indicating a water vapor transport reduction of 40%–50% over the Cascades and Rockies. The QT_{vap} calculated on the 1.33-km WRF grid was very similar to the 4-km QT_{vap}; however, more detail is shown through smaller gaps and passes such as Stampede Gap and the Mt. Hood corridor south of Mt. Hood (Fig. 12c).

The IVT sequences and QT_{vap} suggested that 1) the CR Gap was a ''path of least resistance'' through which water vapor transport was largest, and 2) a large proportion of water vapor impinging on the Cascades survived transit over the ridge into eastern Washington and Oregon. With these findings in mind, we used vertical cross sections to explore the total moisture flux across the Cascades (Fig. 13). We also defined four corridors of interest to further investigate water vapor depletion across the Cascades:

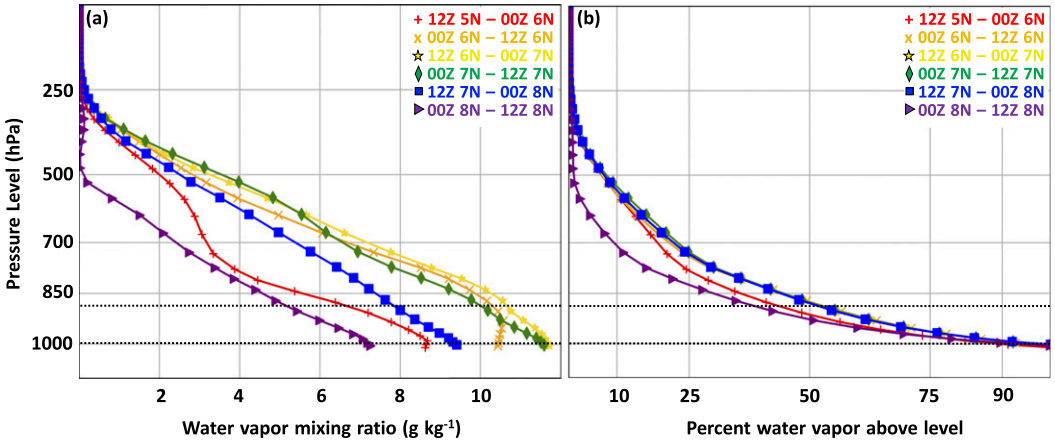

FIG. 9. WRF 4-km vertical profiles of (a) water vapor mixing ratio (in g kg^{-1}) and (b) share of water vapor mass above a specific level above Troutdale, OR (TTD). Profiles are averaged over 12 h. Black dotted lines denote average pressure of (top) the Cascades ridgetop and (bottom) the CR Gorge.

1) the southern Washington Cascades immediately north of the CR Gorge (WaCas);
2) the CR Gap itself (CRG);
3) the relatively low (1000–1250 m) and narrow (60–80 km) ridge immediately south of Mt. Hood [Mt. Hood corridor (MHC)]; and
4) the southern Oregon Cascades (SOrCas).

b. *Moisture mass transport*

Vertical cross sections showed the 1.33-km QTV_{vap} and $uQTV_{vap}$ during the primary AR event in terms of mass per 1.33-km-wide grid cell per 25-hPa-thick layer (Fig. 14). Although some QTV_{vap} depletion occurred across the Cascades (W–W′ to E–E′), most of the moisture appeared to survive the transit: maximum QTV_{vap} was 3000–3500 kg on both sides of the barrier. At the ridge, larger values of QTV_{vap} (>3500 kg) were detected as water vapor was squeezed in the vertical and horizontal by the higher terrain and the narrow CR Gap. The largest values of QTV_{vap} were concentrated through the CR Gap and over the northern OR Cascades.

For ~8 h near the beginning of the primary AR event, winds through the CR Gorge were easterly (see Fig. 6). We explored the possibility that easterly low-level winds were causing negative water vapor transport. We found that any such impact was small compared to the large positive transport values that occurred over the remainder of the 72-h event. Cross sections of $uQTV_{vap}$ show that zonal transport was robust ($uQTV_{vap}$ > 2000 kg); however, comparisons with the notably more-robust QTV_{vap} imply that meridional transport was important as well.

To better understand how much water vapor was crossing the Cascades, we summed QT_{vap} and QT_{mois} along each cross section (Fig. 15). Two clear findings were that 1) the majority (91.5%–97.5%) of transported moisture was in the form of water vapor, and 2) the majority (90.4%) of moisture transport depletion occurred along the western slopes of the Cascades (i.e., on transit from W–W′ to R–R′). Only 9.6% of moisture transport loss occurred east of the Cascades ridge. A more subtle finding was the slight rebound of water vapor on transit from R–R′ to E–E′. While moisture transport continued to decline east of the ridge (though much less rapidly than west of the ridge), water vapor transport increased. The increase was likely due to sinking, drying air east of the Cascades reabsorbing water vapor mass from evaporating/sublimating hydrometeor mass.

Since only 9.6% of moisture transport loss occurred east of the Cascades, the ridge cross section R–R′ was a valuable tool to assess where moisture penetrated the barrier. Based on the terrain, we selected six segments (A, B, C, D, F, and G; see Fig. 13) to analyze. We calculated QT_{mois} and QT_{vap} through each segment (Fig. 16). Results showed most moisture and water vapor transport occurred over the Cascades north and south of the CR Gap (segment D). In fact, only 15.4% of total moisture (QT_{mois}: 3.78×10^{13} vs 24.6×10^{13} kg) and 15.5% of water vapor (QT_{vap}: 3.49×10^{13} vs 22.5×10^{13} kg) was transported through the CR Gap; the rest (~84%) moved over the Cascades ridge. Since each segment varied in width, we calculated the average moisture and water vapor transport per kilometer. This showed the most concentrated moisture transport was centered on segments D and F (CR Gap and Mt. Hood corridor) with lesser values north and south.

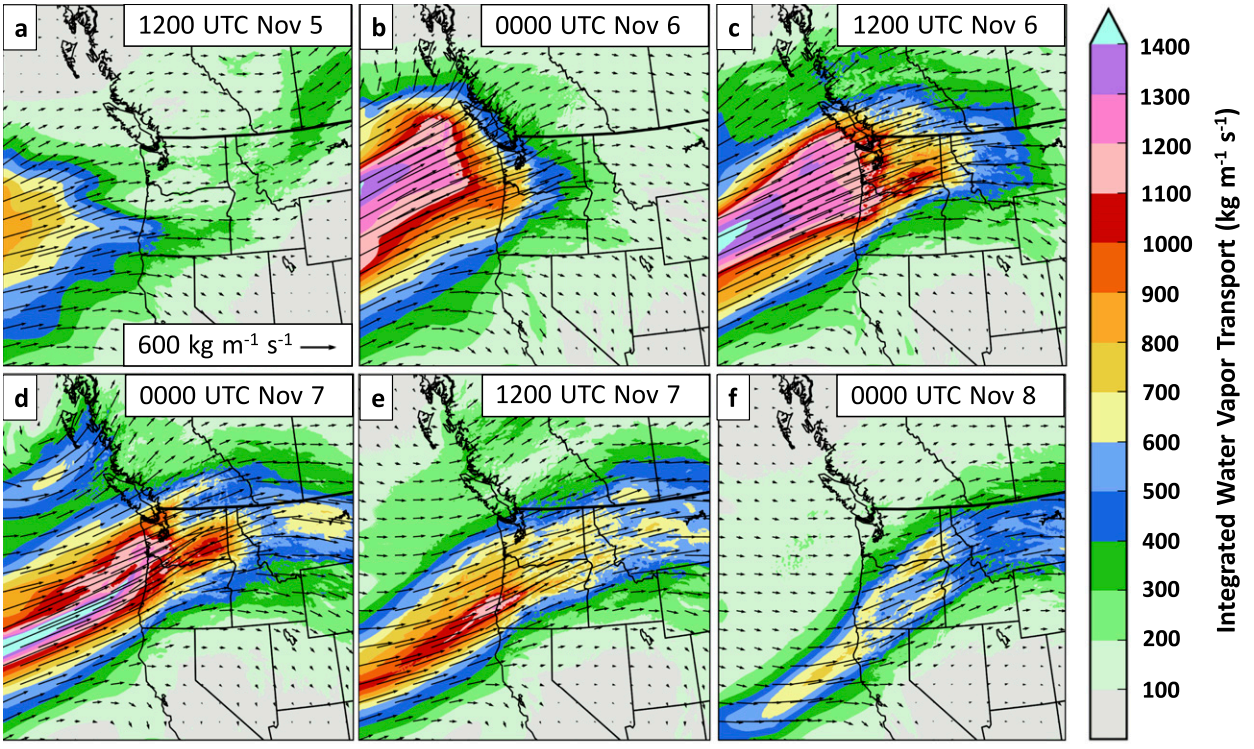

FIG. 10. As in Fig. 8, but for integrated water vapor transport (IVT, in kg m^{-1} s^{-1}). Shading represents IVT magnitude, while vectors denote magnitude and direction.

c. IWT and drying ratios

We calculated IWT to assess total moisture flux (i.e., hydrometeor flux in addition to water vapor flux) and penetration efficiency through the chosen corridors—WaCas, CRG, MHC, and SOrCas. A plan view time series of IWT (not shown) revealed a strikingly similar spatial pattern compared to IVT with increased values (up to 400 kg m^{-1} s^{-1} larger) in areas of clouds and precipitation. Time series plumes of area-averaged IWT showed the weaker antecedent AR followed by the primary AR (Fig. 17). Peak IWT values through the three northernmost corridors exceeded 1500 kg m^{-1} s^{-1} (upstream) and 950 kg m^{-1} s^{-1} (downstream). As previously noted, the AR weakened and moved southward during the second half of the event. The southward

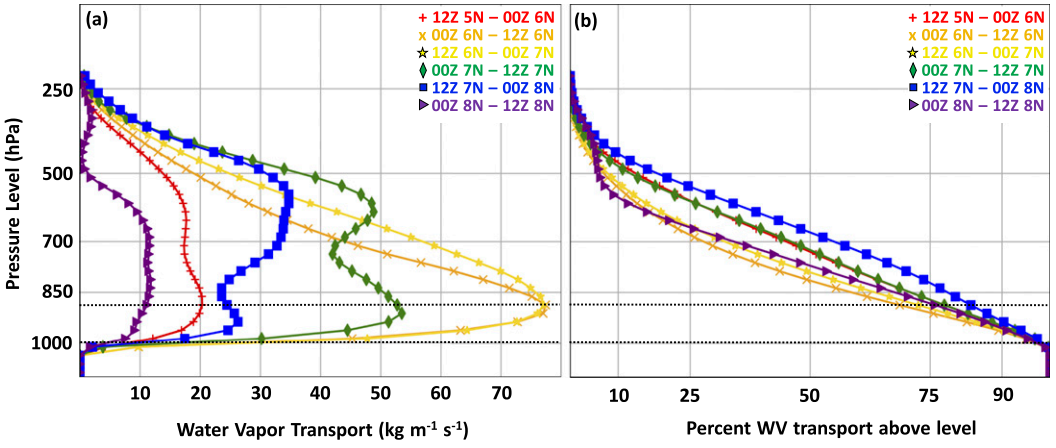

FIG. 11. As in Fig. 9, but for water vapor transport (in kg m^{-1} s^{-1}).

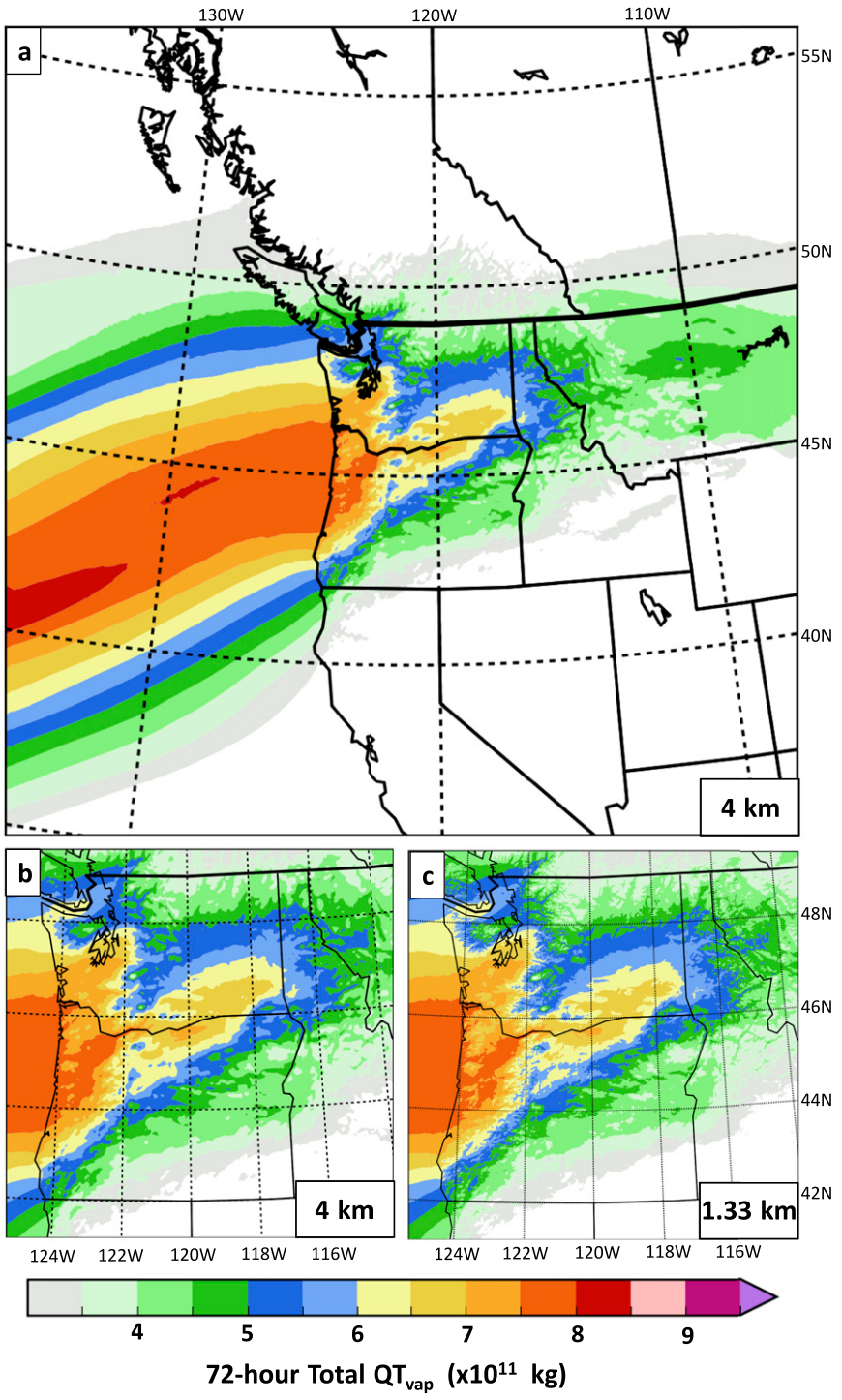

FIG. 12. Water vapor mass transport (QT_{vap}, in kg) during the primary AR during 1200 UTC 5 Nov–1200 UTC 8 Nov: (a) full domain 4-km WRF data, (b) 4-km WRF data zoomed to inner domain extent, and (c) full domain 1.33-km WRF data.

migration and weakening was apparent when comparing the SOrCas IWT time series (peak upstream IWT was 1100 $m^{-1} s^{-1}$; peak downstream IWT was 700 $kg\,m^{-1} s^{-1}$) to those of the corridors farther north.

Downstream IWT values were predictably lower than those upstream of the Cascades due to moisture depletion via precipitation. We quantified moisture depletion through each corridor by calculating drying

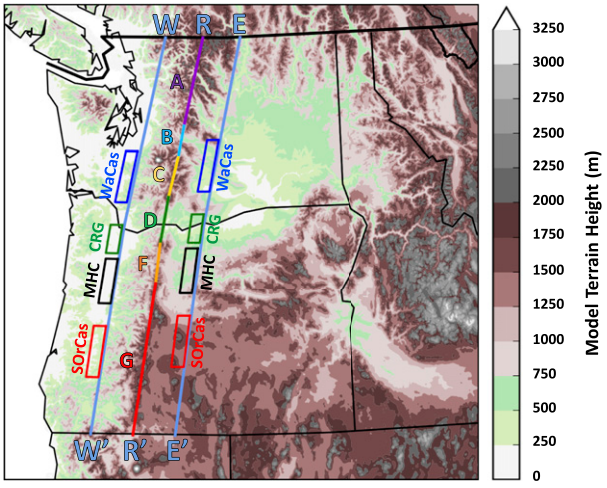

FIG. 13. Corridors of interest for moisture penetration. Cross sections of W–W′, R–R′, and E–E′ were used to plot the vertical moisture structure of the AR and calculate the total moisture flowing through the Pacific Northwest. Corridor boxes WaCas, CRG, MHC, and SOrCas were used to plot IWT temporal plumes and calculate drying ratios. Cross-sectional segments A, B, C, D, F, and G were used to calculate total moisture moving over the ridge. Terrain data are from 1.33-km WRF.

ratios (Fig. 18). Drying ratios indicated the path through the CR Gap (9.3% over the entire simulation) impeded moisture transport less than paths over adjacent terrain (19.6%–30.6% over the entire simulation). Interestingly, drying ratios fell through each corridor during the primary AR (1200 UTC 5 November–1200 UTC 8 November). During the primary AR event, drying ratios through the CR Gap dropped to 3.3% with values of 11.2%–17.3% elsewhere. Moisture transport across the Cascades was most efficient through the CR Gap and least efficient over the SOrCas corridor.

Perhaps the most robust finding was the relatively low drying ratios up and down the Cascades. During the primary AR, cross-barrier moisture reductions were less than 16% from central Washington to central Oregon. Even through the SOrCas corridor, drying ratios were less than 18% during the AR event. The vast majority (~83%–89%) of moisture that impinged on the Cascades during the primary AR event survived transit beyond the mountain ridge. Over 96% of moisture impinging on the CR Gap during the primary AR survived transit through that corridor.

These quantities are similar to the amount of water vapor transport above ridgeline. During the primary AR above Troutdale, 75%–80% and 95% of water vapor transport occurred above the average Cascades ridge height and CR Gap corridor height, respectively (see Fig. 11b). This suggests a strong connection between the vertical depth of water vapor transport and water vapor penetration efficiency.

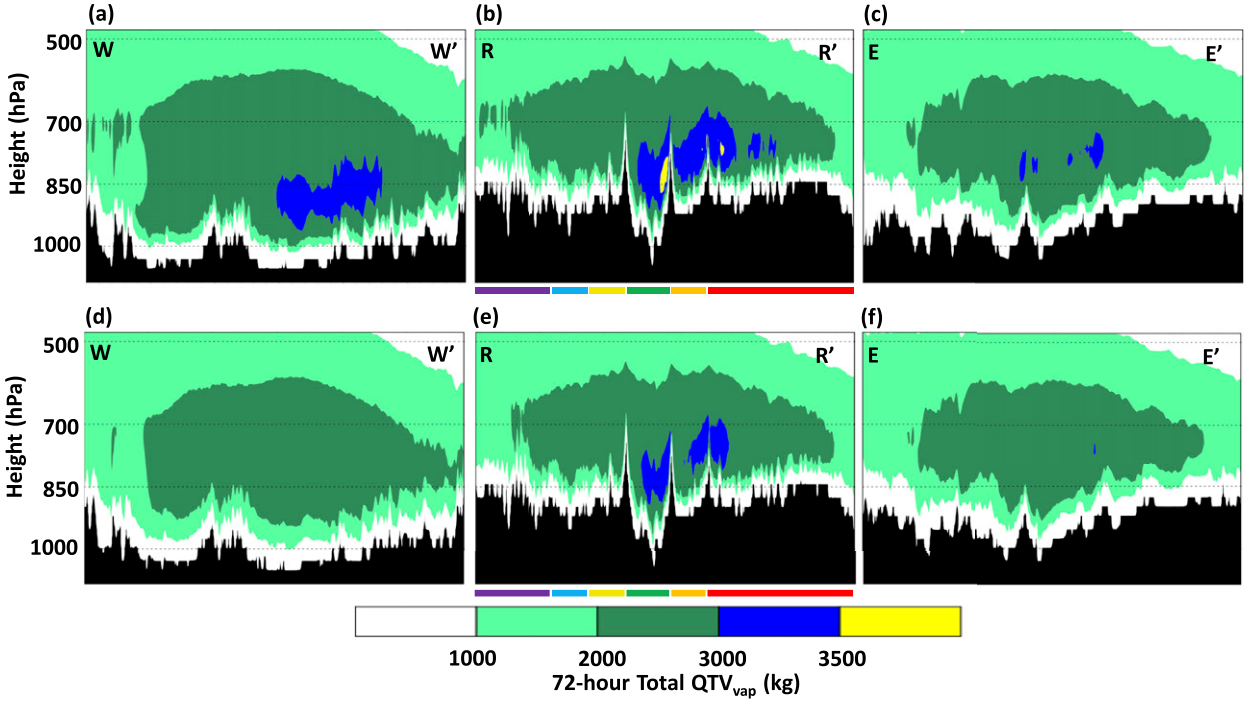

FIG. 14. Vertical cross sections of W–W′, R–R′, and E–E′ showing time-integrated WRF 1.33-km (a)–(c) QTV_{vap} (in kg) and (d)–(f) $uQTV_{vap}$ during 1200 UTC 5 Nov–1200 UTC 8 Nov. Segments A, B, C, D, F, and G along the Cascades are denoted by purple, blue, yellow, green, orange, and red bars below cross section R–R′, respectively.

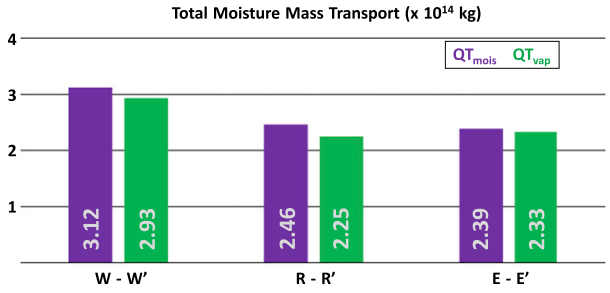

FIG. 15. Total 72-h QT_{vap} and QT_{mois} through cross sections of W–W′, R–R′, and E–E′ during 1200 UTC 5 Nov–1200 UTC 8 Nov. Calculations using 1.33-km WRF. Units are in kg.

5. Conclusions

In this study, we used 4- and 1.33-km gridded model datasets to investigate inland moisture penetration through the U.S. Pacific Northwest during an intense landfalling atmospheric river (AR) event in early November 2006. This particular case was chosen because it caused destructive flooding and record-setting rainfall at interior locations such as Montana's Glacier National Park. Since interior flooding and disaster response are critical to the forecast and emergency management communities of northern Idaho and western Montana, we set out to answer fundamental questions about the inland-penetrating AR. Specifically, we sought to 1) identify corridors through the Cascades that facilitate inland moisture penetration, 2) quantify moisture transport through the corridors, and 3) quantify moisture depletion through the corridors.

To address these questions, we used a 2-domain nested configuration of the Advanced Research Weather Research and Forecasting (WRF-ARW) modeling system to generate a high-resolution realization of the atmosphere during 0000 UTC 3 November–0000 UTC 9 November 2006. We calculated moisture diagnostics such as integrated water vapor (IWV), integrated water vapor transport (IVT), integrated water transport (IWT), water vapor mass transport (QT_{vap}), total moisture mass transport (QT_{mois}), and drying ratios (Kirshbaum and Smith 2008) to probe moisture transport and depletion through the Pacific Northwest.

Before the model datasets were used to address these questions, model precipitation was verified against an observation-based dataset (Livneh et al. 2013). The distribution and magnitude of record-setting precipitation were adequately portrayed by the model. In addition, model 10-m wind speed and direction were verified against observations at six critical locations near the Columbia River Gorge (CR Gorge), Stampede Gap, and the Columbia River basin (CRB). Model data (on both 4- and 1.33-km grids) and observations were similar for both wind speed and direction. Wind data also showed an ~8 h period of light easterly winds preceding the primary AR impact, a common phenomenon in and

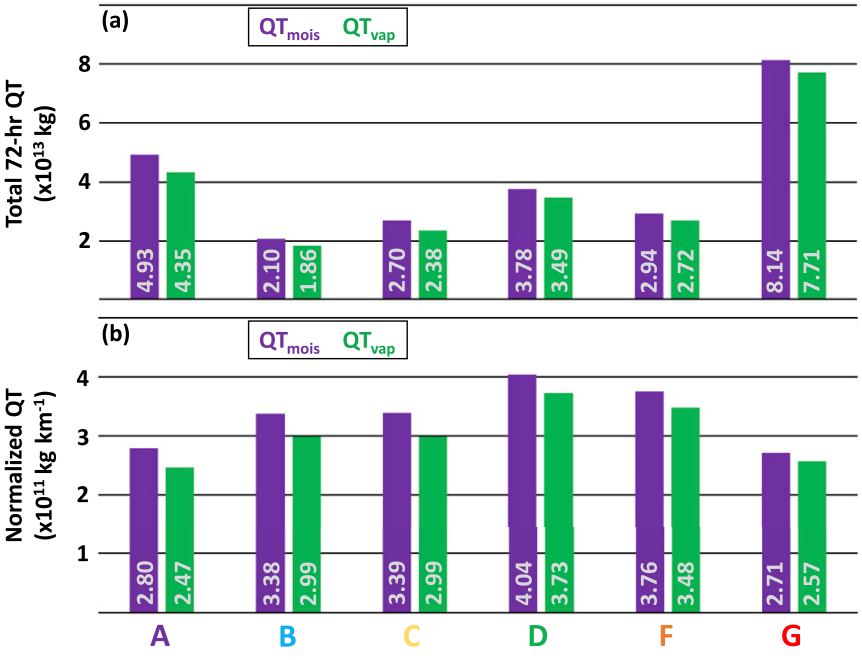

FIG. 16. Total 72-h QT_{vap} and QT_{mois} through cross-sectional segments of R–R′. The locations of segments are shown in Fig. 13. Calculations using 1.33-km WRF. Units are in (a) kg and (b) kg km^{-1}.

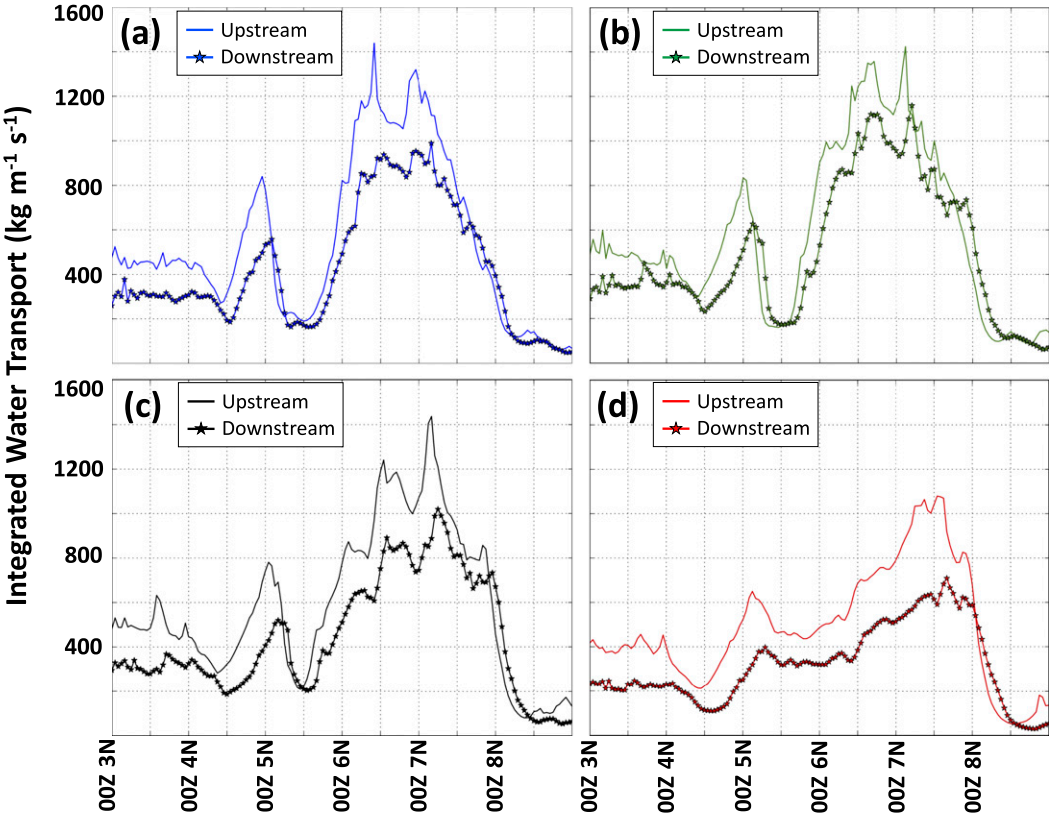

FIG. 17. IWT (in kg m^{-1} s^{-1}) time series through corridors (a) WaCas, (b) CRG, (c) MHC, and (d) SOrCas as defined in Fig. 13. Calculations using 1.33-km WRF. Solid lines denote IWT upstream of the Cascades; starred lines denote IWT downstream of the Cascades.

just west of the CR Gorge (e.g., Sharp and Mass 2002). Because of its favorable performance against precipitation and wind verification data, the model dataset was judged to be sufficiently realistic for the moisture transport analysis.

The fine 1.33-km domain showed more defined easterlies through the CR Gorge on an hourly basis (not shown); however, 12-hourly averaged zonal winds and point observations near the gorge indicate that both 4- and 1.33-km simulations were qualitatively similar. That is, the easterlies through the gorge occurred at the same time on both grids, though less defined in the coarser grid than the finer grid. Furthermore, similarities between the two grids extended to moisture transport calculations (see Fig. 12). Although we showed results on the 1.33-km grid, calculations were qualitatively unchanged on the 4-km grid.

While IWV, IVT, and QT_{vap} plan views and QTV_{vap} cross sections suggested the CR Gap (i.e., the lower terrain between Mt. Adams and Mt. Hood) and the Mt. Hood corridor just south of Mt. Hood comprised a ''path of least resistance'' through the Cascades, it was also apparent that a large proportion of inland-penetrating moisture was moving over the Cascades ridge. We further investigated moisture transport over the Cascades ridge by calculating total QT_{vap} and QT_{mois} over different segments of the ridge. Only ~16% of total cross-Cascades transport moved through the CR Gap; the remainder moved over the Cascades ridge. Though there were no dominant corridors of moisture penetration during this case, normalized QT_{mois} and QT_{vap} indicated the moisture transport through the CR Gap and Mt. Hood Corridor was more intense than anywhere else.

We used drying ratios to examine the proportion of moisture transport (IWT) lost during transit through four corridors over the Cascades. Drying ratios clearly indicated the most efficient (i.e., minimal moisture loss) pathway across the Cascades was through the CR Gap. Moisture transport through the CR Gap was more efficient than over surrounding terrain by a factor of 2–3. During the 72-h primary AR period, drying ratios fell considerably through each corridor.

The reduced drying ratios during the primary AR were unsurprising given that most of the water vapor transport during that time occurred above the average Cascades ridge height. As water vapor transport

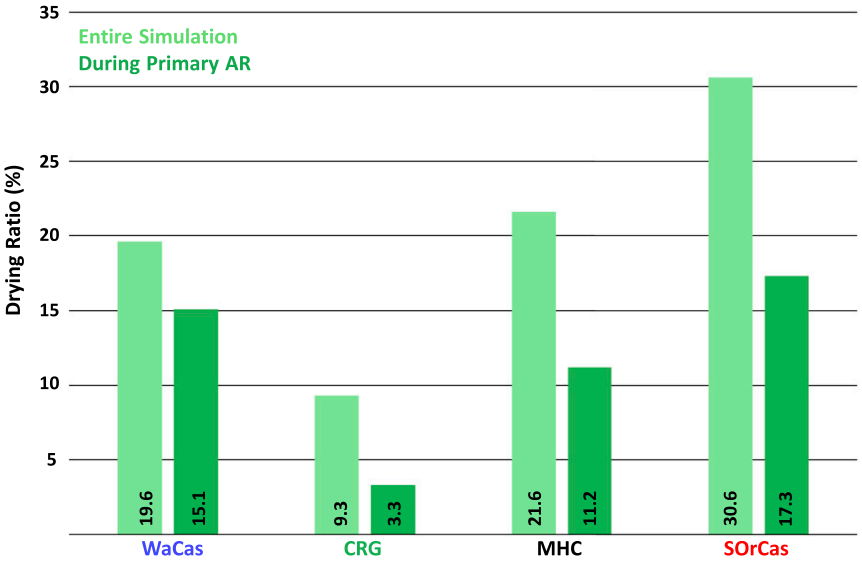

FIG. 18. Drying ratios through each corridor defined in Fig. 13. Calculations using 1.33-km WRF. Drying ratios varied with time during the simulation. Light green bars represent drying ratios during the 144-h simulation; dark green bars represent drying ratios during the 72-h primary AR event (1200 UTC 5 Nov–1200 UTC 8 Nov).

increased, so too did the vertical depth of water vapor transport. The AR evolved from predominantly low-level transport to midlevel transport. Low- and midlevel transport were associated with wind maxima at those levels, common structures associated with ARs as presented in a recent climatology focusing on Sierra Nevada precipitation events (Backes et al. 2015). In addition to the results of our case study and the Sierra Nevada climatology, the idealized study presented in Kirshbaum and Smith (2008) showed a connection between stronger moisture transport and increased efficiency of inland moisture penetration. These results indicate the vertical distribution of moisture transport—both moisture and wind components—is an important factor when assessing the likelihood of water vapor and moisture penetration over terrain.

Drying ratios and moisture transport plan views also suggested terrain east of the Cascades was important for the routing of moisture emerging from transport across the barrier. The CRB in eastern Washington and extreme northern Oregon strongly contrasts with elevated terrain in much of eastern Oregon. Enhanced moisture existed in the CRB after moving beyond the Cascades. Elevated terrain in much of eastern Oregon prevents air from sinking and drying as much as air passing over the relatively narrow ridge west of the CRB. The consistently higher elevation there may support more hydrometeor mass retention and precipitation east of the Cascades, increasing drying ratios. Another possibility for higher drying ratios in southern Oregon is that moisture transport was weakening within the AR as it moved into the region. As noted previously, reduced upwind moisture transport was associated with higher drying ratios across each of the four corridors through the Cascades.

Future studies may use a longer-term (e.g., seasonal) dataset of high-resolution model ARs to test the dependence of inland moisture penetration on AR orientation, strength, and vertical structure in the Pacific Northwest. A similar concept was employed by Hughes et al. (2014) using a linearized model to vary AR orientation penetrating the Baja Peninsula in Mexico. Such a long-term model dataset could also be used to test the relationship between AR strength and penetration efficiency (i.e., drying ratios).

Important questions concerning the impact of AR orientation, strength, and vertical structure in the Pacific Northwest have been raised by this research. Interactions between an AR and the complex terrain in this region are, to some extent, specific to the region and may not be entirely applicable to other regions. This final point is the primary benefit of using high-resolution case studies as a strategy to examine ARs; while there are universal attributes of ARs and climatologies of inland penetration are extremely helpful for forecasters and emergency personnel, it is essential to consider the unique complexities of each region and AR.

Acknowledgments. The authors thank Dr. Michael Alexander for reviewing the manuscript and offering

advice that helped greatly improve it. Paul Neiman offered valuable insight into the historical context of the November 2006 AR event. We also thank two anonymous reviewers for their comments and suggestions that helped to significantly improve the manuscript. This work utilized the Janus supercomputer, which is supported by the National Science Foundation (Award CNS-0821794) and the University of Colorado Boulder. The Janus supercomputer is a joint effort of the University of Colorado Boulder, the University of Colorado Denver, and the National Center for Atmospheric Research. This research was funded through a cooperative agreement between CIRES and the Bureau of Reclamation.

REFERENCES

Alexander, M. A., J. D. Scott, D. Swales, M. Hughes, K. Mahoney, and C. A. Smith, 2015: Moisture pathways into the U.S. Intermountain West associated with heavy winter precipitation events. *J. Hydrometeor.*, **16**, 1184–1206, doi:10.1175/JHM-D-14-0139.1.

Backes, T. M., M. L. Kaplan, R. Schumer, and J. F. Mejia, 2015: A climatology of the vertical structure of water vapor transport to the Sierra Nevada in cool season atmospheric river precipitation events. *J. Hydrometeor.*, **16**, 1029–1047, doi:10.1175/JHM-D-14-0077.1.

Behrangi, A., B. Guan, P. J. Neiman, M. Schreier, and B. Lambrigtsen, 2016: On the quantification of atmospheric rivers precipitation from space: Composite assessments and case studies over the eastern North Pacific Ocean and the western United States. *J. Hydrometeor.*, **17**, 369–382, doi:10.1175/JHM-D-15-0061.1.

Bernhardt, D., 2006: Glacier National Park flooding November 2006. NWS Western Region Tech. Attachment 08-23, 15 pp.

Dettinger, M. D., 2004: Fifty-two years of Pineapple-Express storms across the west coast of North America. California Energy Commission PIER Energy-Related Environmental Research Rep. CEC-500-2005-004, Sacramento, CA, 15 pp.

——, 2013: Atmospheric rivers as drought busters on the U.S. West Coast. *J. Hydrometeor.*, **14**, 1721–1732, doi:10.1175/JHM-D-13-02.1.

——, F. M. Ralph, T. Das, P. J. Neiman, and D. Cayan, 2011: Atmospheric rivers, floods, and the water resources of California. *Water*, **3**, 445–478, doi:10.3390/w3020445.

Dudhia, J., 1989: Numerical study of convection observed during the winter monsoon experiment using a mesoscale two-dimensional model. *J. Atmos. Sci.*, **46**, 3077–3107, doi:10.1175/1520-0469(1989)046<3077:NSOCOD>2.0.CO;2.

Ek, M. B., K. E. Mitchell, Y. Lin, E. Rogers, P. Grummann, V. Koren, G. Gayno, and J. D. Tarpley, 2003: Implementation of Noah land surface model advances in the National Centers for Environmental Prediction operational mesoscale Eta model. *J. Geophys. Res.*, **108**, 8851, doi:10.1029/2002JD003296.

Hong, S.-Y., Y. Noh, and J. Dudhia, 2006: A new vertical diffusion package with an explicit treatment of entrainment processes. *Mon. Wea. Rev.*, **134**, 2318–2341, doi:10.1175/MWR3199.1.

Hughes, M., K. M. Mahoney, P. J. Neiman, B. J. Moore, M. Alexander, and F. M. Ralph, 2014: The landfall and inland penetration of a flood-producing atmospheric river in Arizona. Part II: Sensitivity of modeled precipitation to terrain height and atmospheric river orientation. *J. Hydrometeor.*, **15**, 1954–1974, doi:10.1175/JHM-D-13-0176.1.

Keyser, D., and L. W. Uccellini, 1987: Regional models: Emerging research tools for synoptic meteorologists. *Bull. Amer. Meteor. Soc.*, **68**, 306–320, doi:10.1175/1520-0477(1987)068<0306:RMERTF>2.0.CO;2.

Kirshbaum, D. J., and R. B. Smith, 2008: Temperature and moist-stability effects on midlatitude orographic precipitation. *Quart. J. Roy. Meteor. Soc.*, **134**, 1183–1199, doi:10.1002/qj.274.

Lackmann, G. M., 2013: The south-central U.S. flood of May 2010: Present and future. *J. Climate*, **26**, 4688–4709, doi:10.1175/JCLI-D-12-00392.1.

Lavers, D. A., and G. Villarini, 2013: Atmospheric rivers and flooding over the central United States. *J. Climate*, **26**, 7829–7836, doi:10.1175/JCLI-D-13-00212.1.

——, and ——, 2015: The contribution of atmospheric rivers to precipitation in Europe and the United States. *J. Hydrol.*, **522**, 382–390, doi:10.1016/j.jhydrol.2014.12.010.

Leung, L. R., and Y. Qian, 2009: Atmospheric rivers induced heavy precipitation and flooding in the western U.S. simulated by the WRF regional climate model. *Geophys. Res. Lett.*, **36**, L03820, doi:10.1029/2008GL036445.

Livneh, B., E. A. Rosenberg, C. Lin, B. Nijssen, V. Mishra, K. M. Andreadis, E. P. Maurer, and D. P. Lettenmaier, 2013: A long-term hydrologically based dataset of land surface fluxes and states for the conterminous United States: Update and extensions. *J. Climate*, **26**, 9384–9392, doi:10.1175/JCLI-D-12-00508.1.

Mahoney, K. M., and Coauthors, 2016: Understanding the role of atmospheric rivers in heavy precipitation in the southeast United States. *Mon. Wea. Rev.*, **144**, 1617–1632, doi:10.1175/MWR-D-15-0279.1.

Mlawer, E. J., S. J. Taubman, P. D. Brown, M. J. Iacono, and S. A. Clough, 1997: Radiative transfer for inhomogeneous atmospheres: RRTM, a validated correlated-k model for the longwave. *J. Geophys. Res.*, **102**, 16 663–16 682, doi:10.1029/97JD00237.

Moore, B. J., P. J. Neiman, F. M. Ralph, and F. E. Barthold, 2012: Physical processes associated with heavy flooding rainfall in Nashville, Tennessee, and vicinity during 1–2 May 2010: The role of an atmospheric river and mesoscale convective systems. *Mon. Wea. Rev.*, **140**, 358–378, doi:10.1175/MWR-D-11-00126.1.

——, K. M. Mahoney, E. M. Sukovich, R. Cifelli, and T. M. Hamill, 2015: Climatology and environmental characteristics of extreme precipitation events in the southeastern United States. *Mon. Wea. Rev.*, **143**, 718–741, doi:10.1175/MWR-D-14-00065.1.

Neiman, P. J., F. M. Ralph, G. A. Wick, J. Lundquist, and M. D. Dettinger, 2008a: Meteorological characteristics and overland precipitation impacts of atmospheric rivers affecting the west coast of North America based on eight years of SSM/I satellite observations. *J. Hydrometeor.*, **9**, 22–47, doi:10.1175/2007JHM855.1.

——, ——, ——, Y.-H. Kuo, T.-K. Wee, Z. Ma, G. H. Taylor, and M. D. Dettinger, 2008b: Diagnosis of an intense atmospheric river impacting the Pacific Northwest: Storm summary and offshore vertical structure observed with COSMIC satellite retrievals. *Mon. Wea. Rev.*, **136**, 4398–4420, doi:10.1175/2008MWR2550.1.

——, ——, B. J. Moore, M. Hughes, K. M. Mahoney, J. M. Cordeira, and M. D. Dettinger, 2013: The landfall and inland penetration of a flood-producing atmospheric river in Arizona. Part I: Observed synoptic-scale, orographic, and

hydrometeorological characteristics. *J. Hydrometeor.*, **14**, 460–484, doi:10.1175/JHM-D-12-0101.1.

Newell, R. E., and Y. Zhu, 1994: Tropospheric rivers: A one-year record and a possible application to ice core data. *Geophys. Res. Lett.*, **21**, 113–116, doi:10.1029/93GL03113.

——, N. E. Newell, Y. Zhu, and C. Scott, 1992: Tropospheric rivers? A pilot study. *Geophys. Res. Lett.*, **19**, 2401–2404, doi:10.1029/92GL02916.

Ralph, F. M., P. J. Neiman, and G. A. Wick, 2004: Satellite and CALJET aircraft observations of atmospheric rivers over the eastern North Pacific Ocean during the winter of 1997/98. *Mon. Wea. Rev.*, **132**, 1721–1745, doi:10.1175/1520-0493(2004)132<1721:SACAOO>2.0.CO;2.

——, ——, and R. Rotunno, 2005: Dropsonde observations in low-level jets over the northeastern Pacific Ocean from CALJET-1998 and PACJET-2001: Mean vertical-profile and atmospheric-river characteristics. *Mon. Wea. Rev.*, **133**, 889–910, doi:10.1175/MWR2896.1.

——, ——, G. A. Wick, S. I. Gutman, M. D. Dettinger, D. R. Cayan, and A. B. White, 2006: Flooding on California's Russian River: Role of atmospheric rivers. *Geophys. Res. Lett.*, **33**, L13801, doi:10.1029/2006GL026689.

——, ——, G. N. Kiladis, K. Weickmann, and D. M. Reynolds, 2011: A multiscale observational case study of a Pacific atmospheric river exhibiting tropical–extratropical connections and a mesoscale frontal wave. *Mon. Wea. Rev.*, **139**, 1169–1189, doi:10.1175/2010MWR3596.1.

——, T. Coleman, P. J. Neiman, R. J. Zamora, and M. D. Dettinger, 2013: Observed impacts of duration and seasonality of atmospheric-river landfalls on soil moisture and runoff in coastal northern California. *J. Hydrometeor.*, **14**, 443–459, doi:10.1175/JHM-D-12-076.1.

Ramos, A. M., R. M. Trigo, M. L. R. Liberato, and R. Tomé, 2015: Daily precipitation extreme events in the Iberian Peninsula and its association with atmospheric rivers. *J. Hydrometeor.*, **16**, 579–597, doi:10.1175/JHM-D-14-0103.1.

Rutz, J. J., and W. J. Steenburgh, 2012: Quantifying the role of atmospheric rivers in the interior western United States. *Atmos. Sci. Lett.*, **13**, 257–261, doi:10.1002/asl.392.

——, ——, and F. M. Ralph, 2014: Climatological characteristics of atmospheric rivers and their inland penetration over the western United States. *Mon. Wea. Rev.*, **142**, 905–921, doi:10.1175/MWR-D-13-00168.1.

——, ——, and ——, 2015: The inland penetration of atmospheric rivers over western North America: A Lagrangian analysis. *Mon. Wea. Rev.*, **143**, 1924–1944, doi:10.1175/MWR-D-14-00288.1.

Saha, S., and Coauthors, 2010: The NCEP Climate Forecast System Reanalysis. *Bull. Amer. Meteor. Soc.*, **91**, 1015–1057, doi:10.1175/2010BAMS3001.1.

Sharp, J., and C. Mass, 2002: Columbia Gorge Gap Flow—Insights from observational analysis and ultra-high-resolution simulation. *Bull. Amer. Meteor. Soc.*, **83**, 1757–1762, doi:10.1175/BAMS-83-12-1757.

Skamarock, W. C., and Coauthors, 2008: A description of the Advanced Research WRF version 3. NCAR Tech. Note NCAR/TN-475+STR, 113 pp., doi:10.5065/D68S4MVH.

Smith, B. L., S. E. Yuter, P. J. Neiman, and D. E. Kingsmill, 2010: Water vapor fluxes and orographic precipitation over northern California associated with a landfalling atmospheric river. *Mon. Wea. Rev.*, **138**, 74–100, doi:10.1175/2009MWR2939.1.

Stohl, A., C. Forster, and H. Sodemann, 2008: Remote sources of water vapor forming precipitation on the Norwegian west coast at 60°N—A tale of hurricanes and an atmospheric river. *J. Geophys. Res.*, **113**, D05102, doi:10.1029/2007JD009006.

Thompson, G., P. R. Field, R. M. Rasmussen, and W. D. Hall, 2008: Explicit forecasts of winter precipitation using an improved bulk microphysics scheme. Part II: Implementation of a new snow parameterization. *Mon. Wea. Rev.*, **136**, 5095–5115, doi:10.1175/2008MWR2387.1.

Zhu, Y., and R. E. Newell, 1998: A proposed algorithm for moisture fluxes from atmospheric rivers. *Mon. Wea. Rev.*, **126**, 725–735, doi:10.1175/1520-0493(1998)126<0725:APAFMF>2.0.CO;2.